Effect of Teleconnected Land–Atmosphere Coupling on Northeast China Persistent Drought in Spring–Summer of 2017

DINGWEN ZENG

School of Hydrology and Water Resources, Nanjing University of Information Science and Technology, Nanjing, and Key Laboratory of Regional Climate-Environment for Temperate East Asia, Institute of Atmospheric Physics, Chinese Academy of Sciences, and College of Earth and Planetary Sciences, University of Chinese Academy of Sciences, Beijing, and Key Laboratory of Arid Climatic Change and Reducing Disaster of Gansu Province, and Key Open Laboratory of Arid Climate Change and Disaster Reduction, Institute of Arid Meteorology, China Meteorological Administration, Lanzhou, China

XING YUAN

School of Hydrology and Water Resources, Nanjing University of Information Science and Technology, Nanjing, and Key Laboratory of Regional Climate-Environment for Temperate East Asia, Institute of Atmospheric Physics, Chinese Academy of Sciences, Beijing, China

JOSHUA K. ROUNDY

Department of Civil, Environmental, and Architectural Engineering, University of Kansas, Lawrence, Kansas

(Manuscript received 3 March 2019, in final form 30 July 2019)

ABSTRACT

Northeast China (NEC) suffered a severe drought that persisted from March to July of 2017 with profound impacts on agriculture and society, raising an urgent need to understand the mechanism for persistent droughts over midlatitudes. Previous drought mechanism studies focused on either large-scale teleconnections or local land–atmosphere coupling, while less attention was paid to their synergistic effects on drought persistence. Here we show that the 2017 NEC drought was triggered by a strong positive phase of the Arctic Oscillation in March, and maintained by the anticyclone over the area south to Lake Baikal (ASLB) through a quasi-stationary Rossby wave in April–July, accompanied by sinking motion and north wind anomaly. By using a land–atmosphere coupling index based on the persistence of positive feedbacks between the boundary layer and land surface, we find that the coupling states over NEC and ASLB shifted from a wet coupling in March to a persistently strengthened dry coupling in April–July. Over ASLB, the dry coupling and sinking motion increased surface sensible heat, decreased cloud cover, and weakened longwave absorption, resulting in a diabatic heating anomaly in the lower atmosphere and a diabatic cooling anomaly in the upper atmosphere. This anomalous vertical heating profile led to a negative anomaly of potential vorticity at low levels, indicating that the land–atmosphere coupling had a phase-lock effect on the Rossby wave train originating from upstream areas, and therefore maintained the NEC drought over downstream regions. Our study suggests that an upstream quasi-stationary wave pattern strengthened by land–atmosphere coupling should be considered in diagnosing persistent droughts, especially over northern midlatitudes.

1. Introduction

In March–July of 2017, Northeast China (NEC) suffered its worst spring–summer drought event in recent decades (S. Wang et al. 2019), and this exerted severe impacts on agricultural production and the livelihoods of people, resulting in a direct economic loss of about 7 billion CNY (about one billion U.S. dollars; Zhang et al. 2017). Under the background of decadal variation manifested as ''southern flood–northern drought (Yu et al. 2004; Ding et al. 2009; Wang 2001; Zhou et al. 2009),'' NEC summer precipitation also experienced a decrease after 1999 (Han et al. 2015). Since NEC is one of the major agriculture regions in China, improving the understanding of drought

Supplemental information related to this paper is available at the Journals Online website: https://doi.org/10.1175/JCLI-D-19-0175.s1.

Corresponding author: Xing Yuan, xyuan@nuist.edu.cn

DOI: 10.1175/JCLI-D-19-0175.1

© 2019 American Meteorological Society. For information regarding reuse of this content and general copyright information, consult the AMS Copyright Policy (www.ametsoc.org/PUBSReuseLicenses).

Unauthenticated | Downloaded 01/18/21 09:41 PM UTC

mechanisms is important for both early warning (Yuan and Wood 2013) and disaster mitigation (Li et al. 2019).

In fact, persistent droughts have occurred frequently over different parts of China in recent years. Over southwestern China, a severe drought event occurred with more than 80 dry days in the summer of 2006 (Li et al. 2011), and a drought with the longest period of dry days during a winter season in the past 50 years happened in 2009/10 due to an El Niño event and negative phase of the Arctic Oscillation (Yang et al. 2012). Over East China, teleconnection patterns originating from the North Atlantic contributed to the extreme drought during winter–spring of 2011 (Jin et al. 2013). Over North China, a number of extreme drought events started in spring and persisted into summer, which usually occurred when La Niña transitioned to El Niño with a negative North Pacific oscillation phase in the preceding winter (Chen and Yang 2013; Zhang et al. 2018).

An extreme and prolonged drought event is usually related to local persistent anticyclonic circulation anomaly. This anomaly always appears as a center of certain teleconnection pattern, which is called as the stationary wave pattern (Schubert et al. 2011, 2014). A number of studies investigated the influence of stationary waves on North China drought events. Wei et al. (2004) concluded that droughts in the summers of 1999 and 2000 were attributed to a quasi-stationary wave train over Eurasia (named the EU pattern; Wallace and Gutzler 1981), and Wang et al. (2017) also concluded that the 2015 summer drought was associated with the EU pattern. Wang and He (2015) argued that the 2014 July–August drought was jointly caused by the Silk Road pattern (SR; Lu et al. 2002), the Pacific–Japan pattern (PJ; Nitta 1987), and the EU pattern.

Studies were also carried out to investigate causes of the above teleconnection patterns at different time scales. For the anomaly of stationary Rossby waves at a monthly time scale, submonthly vorticity transients are the primary forcing factors (Schubert et al. 2011). But for the stationary wave anomaly that persists more than one month, the role of external forcing should be considered in addition to internal atmospheric dynamics. For instance, the loss of Barents sea ice in March and subsequent loss of snow cover over western Eurasia in April triggered a polar–Eurasia teleconnection pattern and resulted in the July–August hot drought over NEC in 2016 (Li et al. 2018). The EU pattern triggered by anomalies of Eurasian spring snow and Arctic sea ice cover, the PJ pattern and midlatitude Asian summer pattern associated with sea surface temperature (SST) anomaly over North Pacific and tropical Indo-Pacifc regions, and the SR pattern sustained by intense warming over the European continent synergistically contributed to extreme North China July–August drought (Wang and He 2015; Wang et al. 2017; Xu et al. 2017).

Besides external forcings from the ocean and sea ice, the land surface also plays an important role in sustaining droughts. Correlation analysis showed that soil moisture affected the persistence of droughts through a positive feedback to precipitation, that is, reduced soil moisture decreased evapotranspiration and subsequently reduced precipitation (Wu and Kinter 2009), and this coupling becomes more significant as the time scale increases from daily to monthly (Zeng and Yuan 2018). Moreover, soil moisture can exert a remote impact on precipitation through changing atmospheric circulation. Persistent surface dryness is considered as a quasi-steady heat source and can trigger a Rossby wave pattern that prohibits precipitation, and develops soil moisture anomalies in two regions that can lead to phase locking and an amplification of planetary wave (Koster et al. 2014, 2016).

However, the effects of soil moisture on drought were usually studied from the perspective of feedback between evapotranspiration and precipitation, little attention was paid to the evolution of coupling between soil moisture and the boundary layer, and between the overlying atmospheric dynamic and thermal processes related to persistent drought events. In this study, we aim to answer the following questions: What is the associated anomalous circulation pattern for the persistent 2017 NEC drought? Is there a connection between quasi-stationary Rossby wave train and the persistent NEC drought? What is the role of land–atmosphere coupling in the change of thermal and dynamic structure in the lower atmosphere layer? Can the land–atmosphere coupling be considered as a precursor of atmospheric circulation anomaly, especially in a prolonged drought?

This paper is arranged as follows: data and methods are described in section 2. In section 3a, we investigate the local circulation anomalies and the associated Rossby wave trains that induce the severe drought over NEC during March–July of 2017. In section 3b, we analyze the anomalies of land surface state and atmospheric boundary layer and reveal the evolution characteristics of land–atmosphere coupling during the NEC drought. The feedback of surface diabatic heating to atmosphere circulation is studied by analyzing the potential vorticity (PV) budget in section 3c. In section 3d, we investigate the local precursory signal of the persistent circulation anomalies from soil moisture and land–atmosphere coupling. The results of this study are concluded in section 4.

2. Data and methods

a. *Data*

The datasets derived from ERA-Interim reanalysis (Dee et al. 2011) from 1981 to 2017 were used in this

Unauthenticated | Downloaded 01/18/21 09:41 PM UTC

study, which include 1) daily pressure level data at a horizontal resolution of 1.0° × 1.0° and 2) surface daily data including soil moisture ($m^3\,m^{-3}$) at depths of 0–10 and 0–100 cm, surface sensible heat flux ($W\,m^{-2}$), surface net longwave radiation ($W\,m^{-2}$), surface pressure (Pa), air temperature (K), and specific humidity ($k\,kg^{-1}$) at 2 m. Monthly mean outgoing longwave radiation (OLR) data at a 2.5° × 2.5° grid resolution during 1981–2017 were provided by NOAA (Liebmann and Smith 1996). Monthly gridded precipitation data at 2.5° resolution from NOAA's Precipitation Reconstruction (PREC) data (Chen et al. 2002) were used as observation.

b. Method for characterizing land–atmosphere coupling

Soil moisture can change the surface fluxes and then exert an impact on the atmospheric states through land–atmosphere coupling (Dirmeyer and Halder 2017). Roundy et al. (2013) developed a classification method based on the persistence of positive feedback between evapotranspiration and water vapor in the atmospheric boundary layer, where land–atmosphere coupling states were classified into four types (wet, dry, transitional, and atmospherically controlled) at daily time scales, with both the dry and wet coupling events showing strong persistence. To define the coupling classification, this methodology utilizes a historical dataset of daily convective triggering potential (CTP), low-level humidity index (HI), and soil moisture (SM) taken before dawn. The CTP–HI space is then divided into coupling regimes based on the difference between the climatological distribution of soil moisture and the conditional distribution of soil moisture for specific subspaces in the CTP–HI space. Once the CTP–HI space is classified, a daily coupling regime is defined based on the location of the current day CTP and HI within the classified CTP–HI space. The coupling drought index (CDI) is defined to express the dominant coupling type (dry or wet) over a period of time:

$$\mathrm{CDI} = \frac{N_d - N_w}{N_t}, \tag{1}$$

where N_d, N_w, and N_t refer to the number of dry coupling days, wet coupling days, and total days in the study period. The CDI can be used to link the land–atmosphere dry coupling state at daily time scale with seasonal extreme droughts (Roundy et al. 2013).

CTP ($J\,kg^{-1}$) is the vertical integral of the area between atmospheric temperature profile T_{env} (K) and moist adiabatic T_{parcel} (K) from 100 to 300 hPa (from $Z_{\mathrm{PSurf\text{-}100}}$ to $Z_{\mathrm{PSurf\text{-}300}}$) above surface, and is a measure for boundary layer stability, which is calculated as

$$\mathrm{CTP} = g\int_{Z_{\mathrm{PSurf\text{-}300}}}^{Z_{\mathrm{PSurf\text{-}100}}} \frac{T_{\mathrm{parcel}} - T_{\mathrm{env}}}{T_{\mathrm{env}}}\,dz, \tag{2}$$

where g ($m\,s^{-2}$) is the gravitational acceleration and dz is the thickness (m) of the atmospheric layer, where T_{parcel} is the temperature of air parcel in the moist adiabatic process, which coincides with the constant equivalent potential temperature line. A higher CTP value means a higher boundary layer height and a more unstable boundary layer. HI (K) is defined as

$$\mathrm{HI} = (T_{\mathrm{PSurf\text{-}50}} - T_{d,\mathrm{PSurf\text{-}50}}) + (T_{\mathrm{PSurf\text{-}150}} - T_{d,\mathrm{PSurf\text{-}150}}), \tag{3}$$

which is computed as the sum of the dewpoint depressions (K) in the 50–150-hPa region above ground to measure the wetness of the atmosphere. A lower HI value corresponds to a wetter atmosphere (Findell and Eltahir 2003a). All meteorological variables for calculating HI and CTP are derived from ERA-Interim reanalysis data mentioned in section 2a.

c. Calculations of diabatic heating and PV budget

We calculated the diabatic heating rate Q_1 ($K\,s^{-1}$) as a residual of the thermodynamic equation based on ERA-Interim daily data (Yanai and Tomita 1998; Ren et al. 2015):

$$Q_1 = \frac{\partial T}{\partial t} + \mathbf{V}_h \cdot \nabla_h T + \omega\left(\frac{\partial T}{\partial p} - \frac{RT}{c_p p}\right), \tag{4}$$

where T is the air temperature, $\mathbf{V}_h$ is the horizontal wind in meridional and zonal directions, ω ($Pa\,s^{-1}$) is the vertical velocity at pressure p level, p (Pa) is pressure, R ($\approx 8.314\,J\,mol^{-1}\,K^{-1}$) is the gas constant, c_p ($\approx 1.004\,J\,kg^{-1}\,K^{-1}$) is the specific heat at constant pressure, ∇_h is the horizontal gradient operator, and the unit of Q_1 is converted to kelvins per day ($K\,day^{-1}$) for the later analysis.

To explore the influence of surface sensible heat on atmospheric motion, we calculated the PV. PV can be derived through a combination of the first law of thermodynamics and momentum conservation, because it can only be changed by diabatic heating or frictional processes. The expression of PV in the p coordinate is shown as

$$\mathrm{PV} \cong -g(f + \zeta)\frac{\partial \theta}{\partial p}, \tag{5}$$

where f (s^{-1}) is the Coriolis parameter, ζ (s^{-1}) is vertical relative vorticity, and θ (K) is isobaric potential

Unauthenticated | Downloaded 01/18/21 09:41 PM UTC

temperature. The unit of PV is PVU (1 PVU = $10^{-6}\,\mathrm{K\,kg^{-1}\,m^2\,s^{-1}}$). If diabatic heating is considered and friction is neglected, local variability of PV ($\partial\mathrm{PV}/\partial t$) is determined by three terms: the horizontal and vertical advections, and diabatic heating. The corresponding equation is

$$\frac{\partial \mathrm{PV}}{\partial t} = \underbrace{-\left(u\frac{\partial \mathrm{PV}}{\partial x} + v\frac{\partial \mathrm{PV}}{\partial y}\right)}_{\text{part-h}} \underbrace{-\omega\frac{\partial \mathrm{PV}}{\partial p}}_{\text{part-w}} \underbrace{-g(f+\zeta)\frac{\partial Q_1}{\partial p}}_{\text{PVG}} - g\left(\zeta_x\frac{\partial Q_1}{\partial x} + \zeta_y\frac{\partial Q_1}{\partial y}\right), \quad (6)$$

where ζ_x and ζ_y are the zonal and meridional components of relative vorticity, respectively. On the right side of the equation, the first two terms are the PV variation caused by horizontal (part-h) and vertical (part-w) movement. The third term represents PV variability generated by vertical gradient of Q_1 and absolute vorticity, and is denoted as PVG hereafter. The fourth term is the same as the third, but for the horizontal direction, which is much smaller than the others and can be neglected. Similar to Ren et al. (2015), we decomposed a daily mean variable into its long-term average (denoted with an overbar and named as basic flow hereafter) and interannual components. The first three terms on the right side of Eq. (6) can be modified into the following:

$$\mathrm{PV}'_{\text{part-h}} = -\left(\overline{u}\frac{\partial \mathrm{PV}'}{\partial x} + \overline{v}\frac{\partial \mathrm{PV}'}{\partial y}\right) - \left(u'\frac{\partial \overline{\mathrm{PV}}}{\partial x} + v'\frac{\partial \overline{\mathrm{PV}}}{\partial y}\right) + \mathrm{residues}_h, \quad (7)$$

$$\mathrm{PV}'_{\text{part-w}} = -\overline{\omega}\frac{\partial \mathrm{PV}'}{\partial p} - \omega'\frac{\partial \overline{\mathrm{PV}}}{\partial p} + \mathrm{residues}_w, \quad \text{and} \quad (8)$$

$$\mathrm{PV}'_{\mathrm{PVG}} = -g(f+\overline{\zeta})\frac{\partial Q'_1}{\partial p} - g\zeta'\frac{\partial \overline{Q}_1}{\partial p} + \mathrm{residues}_Q, \quad (9)$$

where the first term on the right-hand side of Eq. (9) is the main contributor, which is related to vertical gradient of interannual anomalies of diabatic heating. Therefore, we calculated $-g(f+\overline{\zeta})(\partial Q'_1/\partial p)$ to represent $\mathrm{PV}'_{\mathrm{PVG}}$ hereafter. The residue terms in Eqs. (7)–(9) are very small, and can be neglected.

d. SVD and lag correlation

To identify the lagged covariability relationship between monthly low-level atmosphere (geopotential height at 850 hPa) and antecedent soil moisture anomalies (top 100 cm), the singular value decomposition (SVD) analysis was employed. The relationship between land–atmosphere coupling and atmospheric state (850 hPa) was also studied via lag correlation of regional mean CDI (May–June) with geopotential height and Q_1 (June–July).

3. Results

a. 2017 NEC drought and the associated atmospheric circulations

The evolution of monthly standardized precipitation anomalies during March–July in 2017 with respect to the climatology of 1981–2017 is shown in Figs. 1a–e. There is a clear negative precipitation anomaly over NEC and the area south to Lake Baikal (ASLB) in each month, which indicates a strong persistence of this drought event. The time series of regional average precipitation values during March–July for each year indicates the 2017 drought is the most severe one over NEC since 1981 (Fig. 1f).

To explore the cause for the NEC and ASLB precipitation anomaly during spring–summer of 2017, we analyzed the atmospheric circulation anomaly, and calculated the wave activity flux (Takaya and Nakamura 2001) to characterize the propagation of Rossby wave in the westerlies (Figs. 2a,b). The results show that the anomalous circulation patterns are significantly different between March and April–July. For geopotential height anomaly at 500 hPa, a strong positive anomaly over the high-latitude regions of Eurasia occurred during March (Fig. 2a), especially over the Far East. But a circulation adjustment occurred during April–July (Fig. 2b), where a wave train originated from the Atlantic and propagated to downstream areas, with negative centers over the Atlantic and eastern Europe, and positive centers over the coast of western Europe and ASLB. In fact, the negative anomaly over the polar region and the positive anomaly over mid- and high latitudes in March (Fig. 2a) indicated a strong positive phase of Arctic Oscillation (AO), with an AO index of 1.365. The positive phase of AO accompanied sinking motion and warmer surface due to a more zonally symmetric circulation in high latitudes, which prevented cold air from moving southward (Yin et al. 2013; Thompson and Wallace 1998). The circulation differences between March and April–July were also exhibited in the meridional wind anomalies at 250 hPa (Figs. 2c,d). However, there were abnormal north winds over NEC in both periods, which were displayed in the longitude–time evolution plot around 120°E (Fig. 2e).

A similar circulation pattern was exhibited at 700 hPa (Figs. 3a,b), indicating a quasi-barotropic structure. The climatological mean field of 500-hPa geopotential height shows that NEC is located on the front of the Baikal high ridge and the back of the East Asian trough (Fig. S1 in

Unauthenticated | Downloaded 01/18/21 09:41 PM UTC

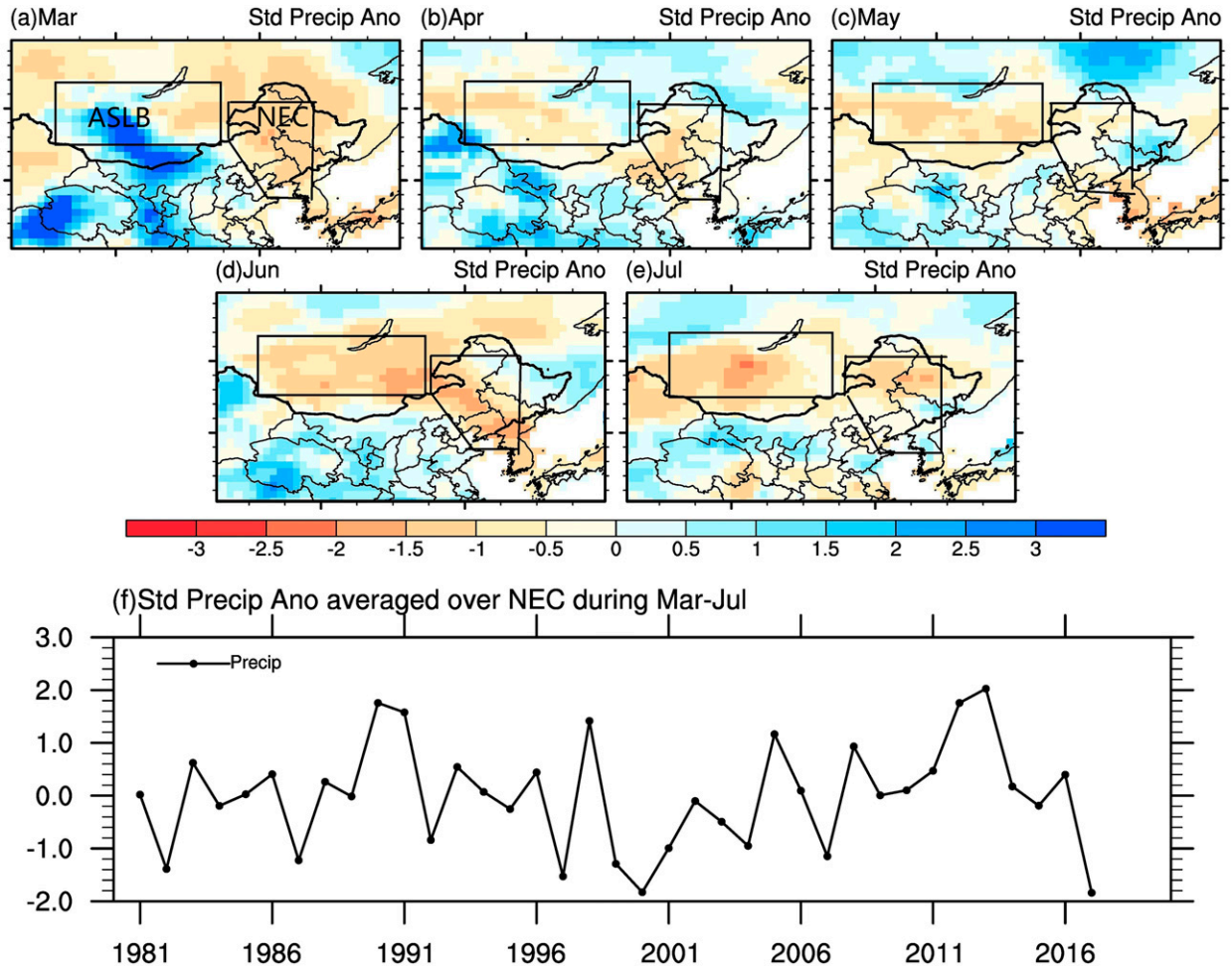

FIG. 1. Standardized precipitation anomalies in (a) March, (b) April, (c) May, (d) June, and (e) July, and (f) the time series of standardized March–July mean precipitation anomalies averaged over the Northeast China (NEC) region marked in Fig. 1a. The area south to Lake Baikal is also marked in Fig. 1a as ASLB.

the online supplemental material), so it is usually dominated by downward motion. The positive geopotential height anomalies in 2017 strengthened the Baikal high ridge and the dynamic descent. The 850-hPa wind anomaly also shows that the high-latitude region was controlled by anticyclone in March (Fig. 3a), but only ASLB was controlled by anticyclone during April–July, resulting in anomalous northerly wind over NEC (Fig. 3b), and the weakened northward moisture transport (Figs. 3c,d). The local meridional–vertical circulation anomaly averaged over 90°–120°E shows that there was an anomalous ascending motion around 45°N in March (Fig. 3e), which matched the area with positive precipitation anomalies in Fig. 1a. However, from April to July, an anomalously sinking motion in the upper-middle troposphere was displayed in the region of 40°–55°N (Fig. 3f). The descending motion to the south of 50°N strengthened the sinking branch of the Ferrel cell (red downward arrow in Fig. 3f, and vectors in Fig. S4), and the descending motion to the north of 50°N weakened the updraft (red upward arrow in Fig. 3f, and vectors in Fig. S4) of the Ferrel cell over ASLB, resulting in negative precipitation anomaly during April–July (Figs. 1b–e).

b. Land–atmosphere coupling during the 2017 persistent drought over NEC and ASLB

The above analysis indicates that the strong positive phase of AO triggered the drought event in March, and the drought was maintained by a wave train originating from the Atlantic with a phase-locked anticyclone over ASLB during April–July. To further explore the possible local influence of land surface conditions on this anticyclone, the coupling feature between soil moisture and atmospheric boundary layer is investigated in this section. Figure 4 shows

Unauthenticated | Downloaded 01/18/21 09:41 PM UTC

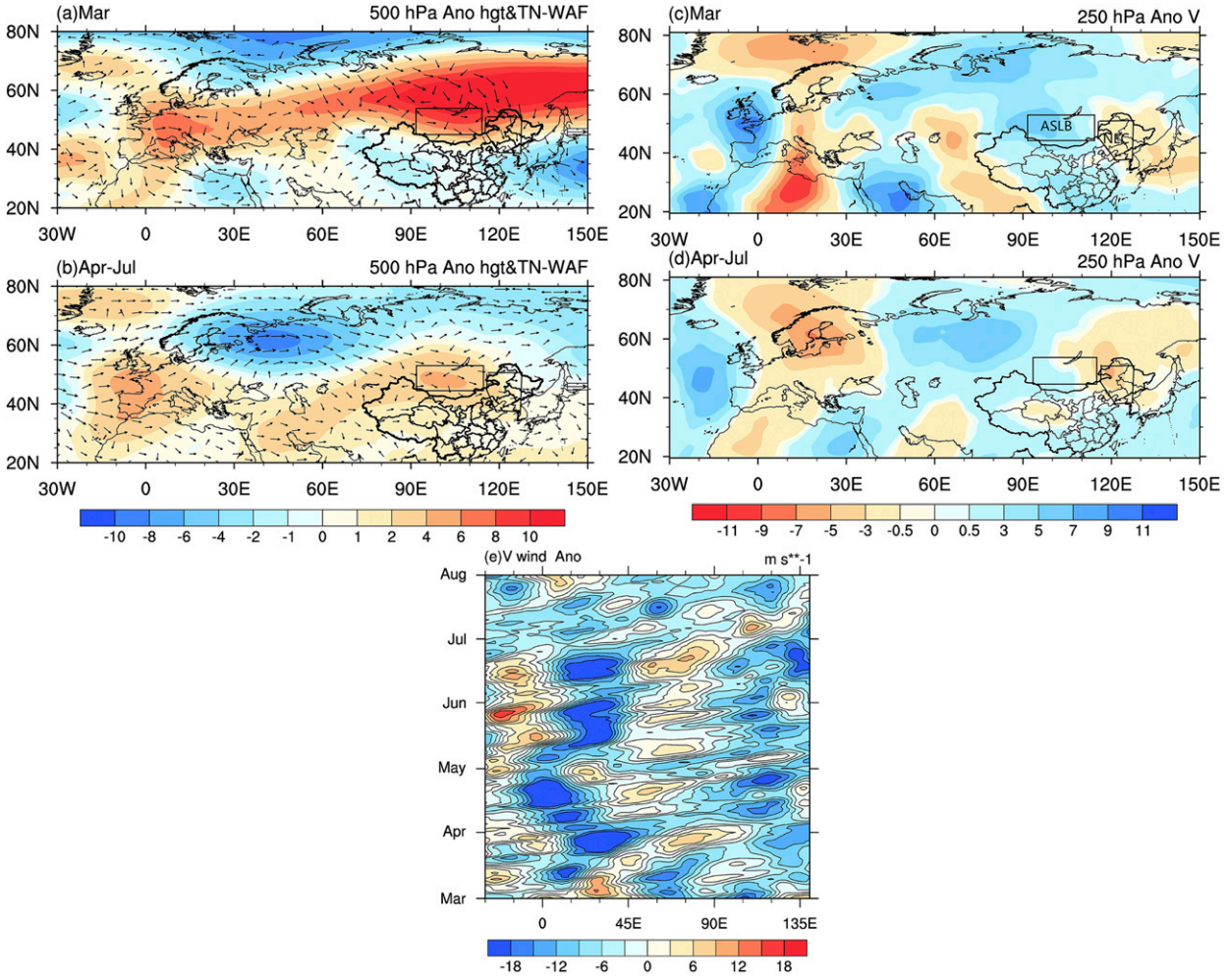

FIG. 2. (a),(b) Geopotential height anomalies (shaded; dagpm) and wave activity flux (vectors; $m^2 s^{-2}$) at 500 hPa in March and April–July during 2017, respectively. (c),(d) The meridional wind anomalies at 250 hPa in March and April–July 2017, respectively. (e) Longitude–time diagram for 15-day running mean of the meridional wind anomalies averaged over 55°–60°N during March–July 2017.

the spatial patterns of anomalies of monthly soil moisture (Figs. 4a–e), HI (Figs. 4f–j), and low-level CTP (Figs. 4k–o) during March–July of 2017. To facilitate the analysis in different months and different regions, the three variables were standardized. Even though there was a negative precipitation anomaly over NEC in March (Fig. 1a), the corresponding SM anomaly was still positive over NEC and was weakly negative over ASLB (Fig. 4a). April is a tipping point, where a weak negative SM anomaly emerged over NEC and an obvious negative anomaly occurred over ASLB (Fig. 4b). The soil drying was intensified in the subsequent three months over the two regions (Figs. 4c–e). A similar turning point was also found in the HI fields. Figures 4f–j show a slightly wetter boundary layer in March with low HI values, while it became drier during April–July over NEC and ASLB with higher HI and a higher lifted condensation level (LCL), suggesting a unfavorable condition for convective precipitation. The analysis of SM and HI implies that the water deficiency in the land surface and atmospheric boundary layer lagged one month behind the negative precipitation anomaly at the onset of the 2017 drought. At daily time scales, a necessary condition for convective triggering is that the boundary layer height is above the LCL (Santanello et al. 2011). In April–July of 2017, the drier soil led to more sensible heat and less evaporation, manifested as strong positive anomaly of CTP (Figs. 4l–o) and positive anomaly of HI (Figs. 4g–j). Although the positive CTP anomaly resulted a well-developed boundary layer, the poor water vapor condition in boundary layer (higher value of HI) and large-scale water vapor flux divergences (Fig. 3d) over the two regions are not in favor of rain; that is, it is too dry for convection to occur.

Unauthenticated | Downloaded 01/18/21 09:41 PM UTC

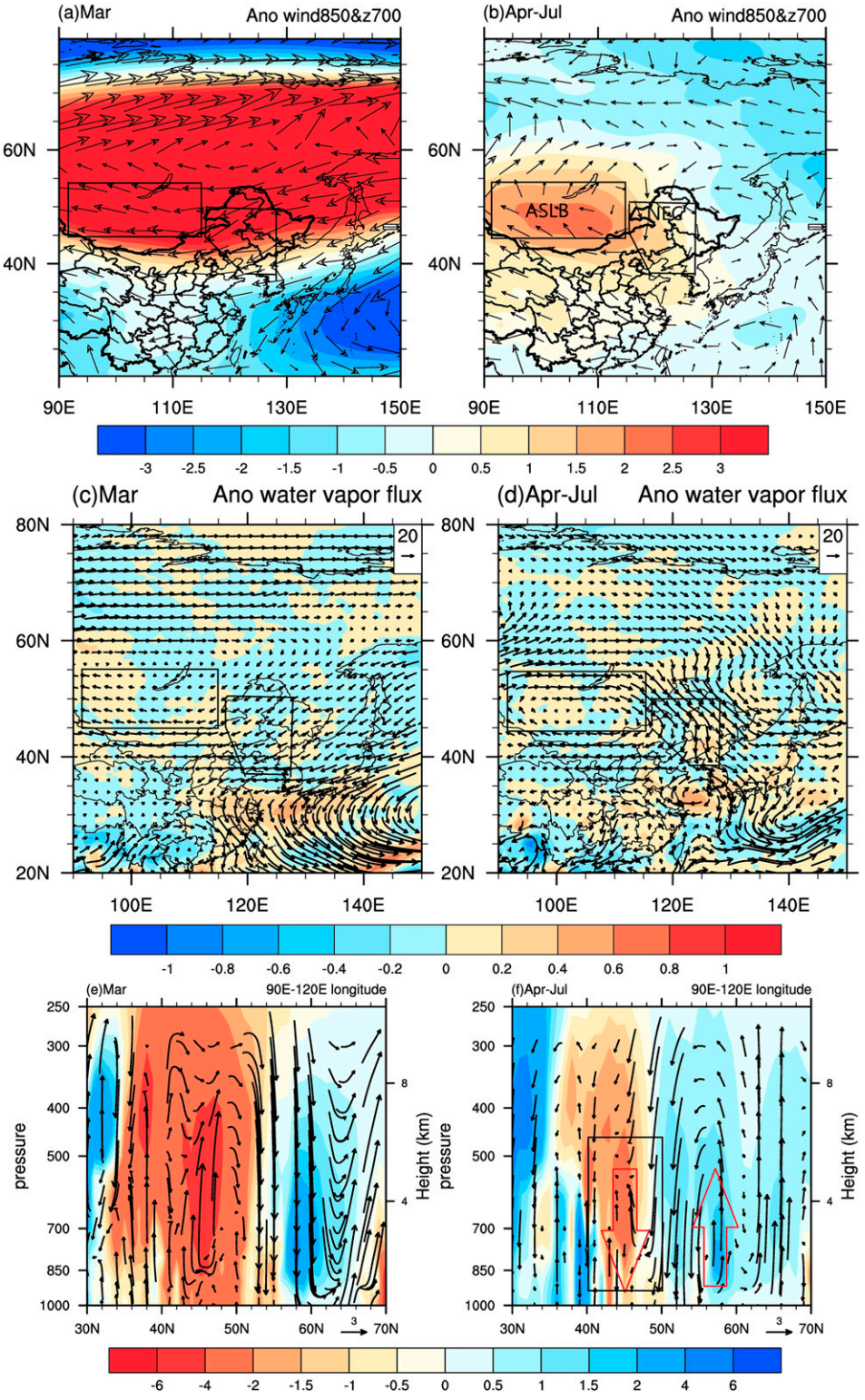

FIG. 3. Geopotential height anomalies at 700 hPa (shaded; dagpm) and the anomalous winds (vectors; m s^{-1}) at 850 hPa in (a) March and (b) April–July during 2017, anomalies of water vapor flux integrated from Earth's surface up to 250 hPa (vectors; kg m^{-1} s^{-1}) and its divergence (shaded; 10^{-4} kg m^{-2} s^{-1}) in (c) March and (d) April–July, and anomalous meridional–vertical circulation averaged over 90°–120°E, with shades indicating the long-term mean of vertical velocity ($-1 \times$ Pa s^{-1}) in (e) March and (f) April–July; the red arrows in (f) represent the climatological mean location of ascending and descending branch of the Ferrel cell and the black box in (f) marks the vertical convergence zone over ASLB.

Unauthenticated | Downloaded 01/18/21 09:41 PM UTC

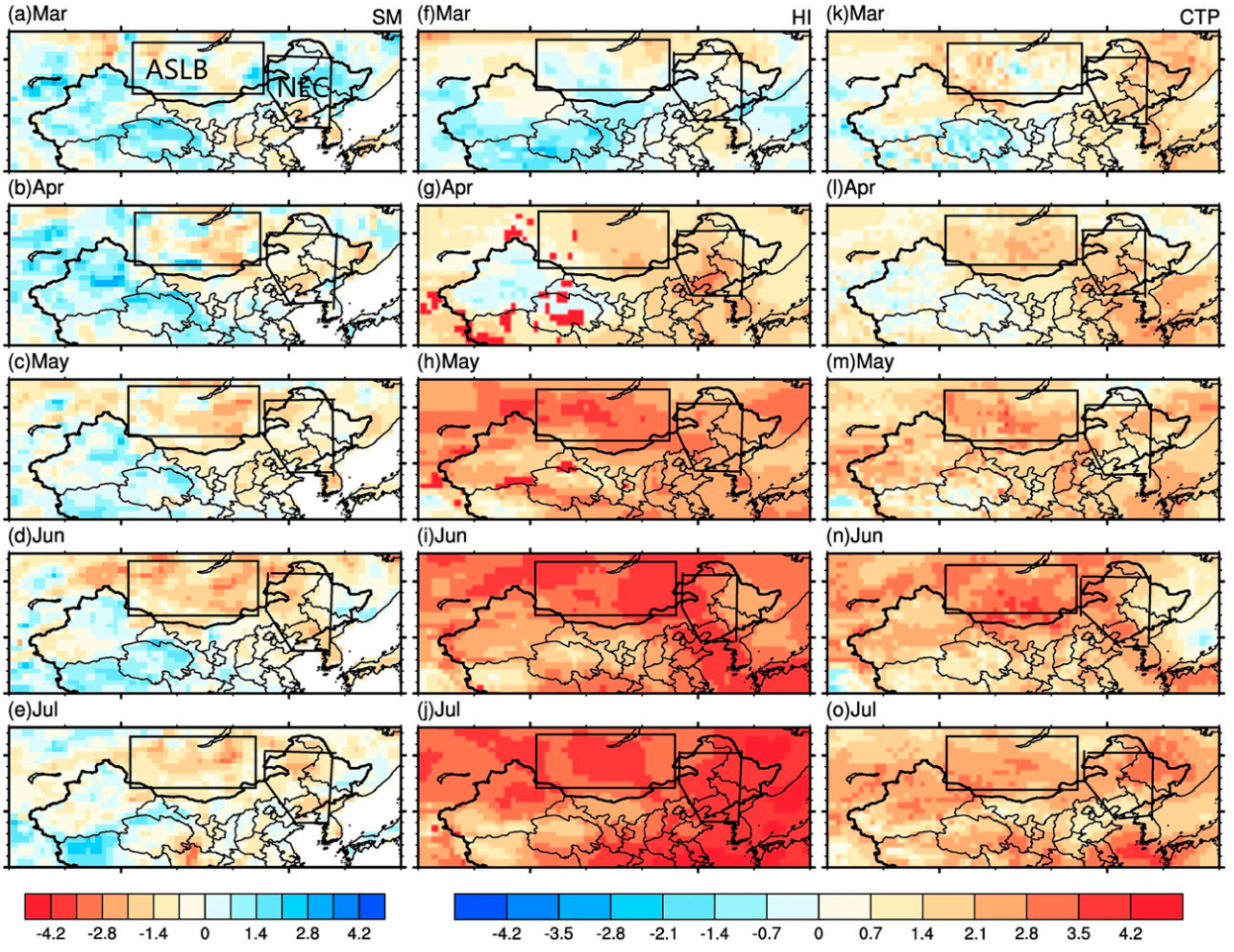

FIG. 4. Standardized anomalies of monthly soil moisture, low-level humidity index (HI), and convective triggering potential (CTP) during March–July 2017.

The dryness of the soil and boundary layer that lasts for a long period of time may be caused by the positive feedback between them. The feedback could be divided into two processes: 1) When under a large-scale circulation background not suitable for raining, a drier boundary layer needs more water vapor from land surface, resulting in large evaporation demand and a drier soil surface. However, the large-scale water vapor divergence consumes the water evaporated from the land surface, reduces the soil water that enters into air, and consequently prohibits precipitation. 2) On the other hand, when under the large-scale circulation background that is suitable for raining, wetter soil can provide sufficient water vapor to the boundary layer to initiate convective precipitation and increase soil moisture. The above two positive feedback processes are classified as dry coupling and wet coupling, respectively, at daily time scales, and they can be characterized in the CTP–HI–SM space summarized by the CDI (Roundy et al. 2013), where a higher (lower) value of CDI means dry (wet) coupling plays a dominant role in the studied time period.

Similar to the temporal evolution of the SM and HI anomaly in 2017, standardized anomalies of CDI also showed a transition from wet coupling in March (Fig. 5a) to dry coupling in April–July (Figs. 5b–e), with the dry coupling gradually strengthening during the evolution of the drought. In accordance with the lowest precipitation of 2017, the regional averaged CDI also shows that ASLB and NEC experienced the driest soil and strongest dry coupling during April–July since 1981 (Figs. 5f,g).

c. *Diabatic heating feedback and its role in maintaining the anticyclone over ASLB*

With the strongest dry coupling over ASLB in 2017 from the above analysis, the lower atmosphere continuously received sensible heating from the surface that

Unauthenticated | Downloaded 01/18/21 09:41 PM UTC

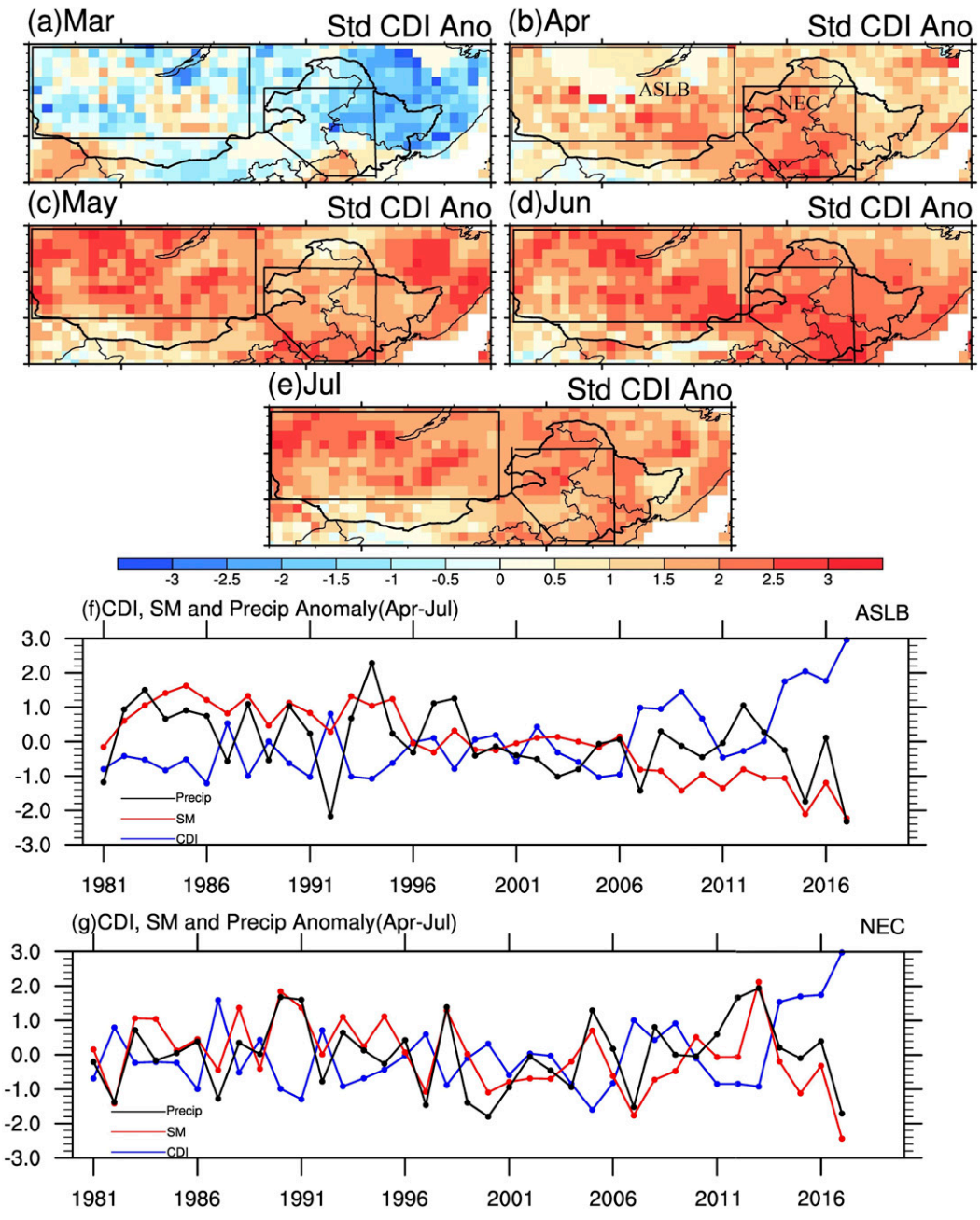

FIG. 5. Standardized anomalies of the coupling drought index (CDI) during (a)–(e) March–July 2017, and time series of standardized April–July mean CDI (blue), soil moisture (red), and precipitation (black) averaged over the (f) ASLB and (g) NEC regions marked in Fig. 5b during 1981–2017.

manifested as a large positive anomaly of CTP (Figs. 4l–o). In fact, the center of the negative SM anomaly and positive CTP anomaly located over ASLB instead of NEC, which matched with the location of anticyclone at 500 and 700 hPa (Figs. 2a, 3a). Whether the persistent anomaly of the dry land surface and associated sensible heating has a feedback to atmospheric circulation requires further investigation. Therefore, in this section, we diagnosed the contributions of the three items [Eqs. (7)–(9)] to the local PV anomaly at 750 hPa during March–July of 2017, especially the dynamic and thermodynamic processes related to the diabatic heating.

Although all terms in Eqs. (7)–(9) are calculated, $PV'_{part\text{-}h}$ [Eq. (7)] is dominated by the first item

Unauthenticated | Downloaded 01/18/21 09:41 PM UTC

$-[\overline{u}(\partial \mathrm{PV}'/\partial x)+\overline{v}(\partial \mathrm{PV}'/\partial y)]$ on the right side of the equation, which represents the horizontal advection of interannual PV anomalies due to basic flow; $\mathrm{PV}'_{\text{part-w}}$ [Eq. (8)] is dominated by the second item $-\omega'(\partial\overline{\mathrm{PV}}/\partial p)$, which represents the vertical advection of basic flow PV anomalies due to interannual anomalies of vertical velocity; $\mathrm{PV}'_{\mathrm{PVG}}$ [Eq. (9)] is dominated by the first item $-g(f+\overline{\zeta})(\partial Q'_1/\partial p)$, which represents the interannual anomalies of the vertical gradient of diabatic heating and basic flow absolute vorticity (figures omitted). This is consistent with the result of Ren et al. (2015). However, to make an accurate comparison, here we still showed the sum of the two terms on right side of Eqs. (7)–(8) in Figs. 6a–d, but the first item of Eq. (9) in Figs. 6e and 6f.

A negative PV anomaly means lower PV or an anticyclonic anomalous system. The negative center of the PV anomaly in 2017 was only located over NEC during March (contours in Figs. 6a, 6c, and 6e) at 750 hPa, but was located over ASLB and NEC during April–July (contours in Figs. 6b, 6d, and 6f), which is consistent with the positive height anomalies at 700 hPa and anticyclonic wind anomalies at 850 hPa (Figs. 3a,b). Based on the analysis of the contributions of three terms to the negative PV anomaly, we find that the horizontal advection (shaded in Figs. 6a and 6b) showed positive anomaly over NEC during March, and weak positive or negative anomalies over ASLB during April–July. The vertical advection (shaded in Figs. 6c and 6d) also showed weak positive or negative anomalies over NEC during March and over ASLB during April–July and is not consistent with the negative PV anomalies. This means both vertical and horizontal items contributed little to the negative PV anomalies, while the anomalous pattern of PVG items (shaded in Figs. 6e and 6f) matched well with the spatial distribution of PV anomaly over NEC and ASLB, indicating the maintenance of negative troposphere PV anomaly is mainly due to PV generation related to diabatic heating. So we calculated the anomalous diabatic heating rates field at 850 hPa as a representation of the thermal state at the low level (shaded in Figs. 6g and 6h), and found that a positive center was located over NEC in March and over ASLB in April–July, which also matched well with the corresponding negative PV anomalies (contours in Figs. 6a–f). Our result showed that positive surface sensible heat anomaly (contours in Figs. 6g and 6h) had a similar distribution as the Q_1. This is in accordance with the previous studies that a surface sensitive heat flux anomaly due to dry soil for a long period of time can be seen as a quasi-steady heat source in the low troposphere (Koster et al. 2016).

According to Eq. (9), PVG is mainly related to the vertical gradient of the Q_1 anomaly, so the vertical heating rate profiles over ASLB during April–July are given in Fig. 7a. There was an anomalous heating between 1000 and 700 hPa with a maximum at 850 hPa, and an anomalous cooling above 700 hPa with a minimum at 600 hPa, this structure of upper cooling and lower heating may lead to a positive vertical gradient ($\partial Q'_1/\partial p$) at 750 hPa. In Eq. (9), $(f+\overline{\zeta})$ is positive in middle and high latitudes, thus leading to a negative PVG during April–July (shaded in Fig. 6f). The diabatic heating in the atmosphere usually comes from precipitation latent heat release, surface sensible heat, and surface longwave radiation. The specific humidity showed strong negative anomaly between 1000 and 650 hPa during April–July of 2017 (Fig. 7b), so the ''low-level heating'' (shaded in Fig. 6h) was mainly due to surface sensible heating anomaly (contours in Fig. 6h). For the ''upper cooling,'' liquid water and water vapor in the clouds can absorb the surface longwave radiation, but significant anomalous air downwelling in April–July (Fig. 3f) led to negative low cloud cover (LCC) anomalies (Fig. 8b) with the increase of net OLR (Fig. 8d). The negative (positive) centers of LCC (OLR) also matched with the anticyclone over ASLB during April–July (Fig. 3b), while their associations were not obvious in March (Figs. 8a,c). Therefore, the clouds absorbed less longwave radiation from the land surface, which manifested as a cooling anomaly above 700 hPa (Fig. 7a). There is a positive vertical gradient of Q'_1 between 850 and 600 hPa (Fig. 7a), so we calculated the vertical integration of PV′, $\mathrm{PV}'_{\text{part-w}}$, $\mathrm{PV}'_{\text{part-h}}$, and PVG from surface to 600 hPa as a representative of the low levels (Fig. S5). The results are similar to those in Fig. 6, but for upper levels (500 hPa), the advection effect ($\mathrm{PV}'_{\text{part-w}}$), rather than PVG, has a strong contribution to the negative anomaly of PV (Fig. S6).

Based on the above analysis, we can conclude that a lot of sensible heat was transported to the lower atmosphere layer during April–July due to persistently increasing dry coupling over ASLB (shaded in Fig. 6h). So there is an ascending motion anomaly at the low level around 850 hPa due to sensible heating, and a descending motion anomaly below 500 hPa due to the teleconnection. This is clearly shown in the black box region of Fig. 3f. Thus the upper descending and lower ascending lead to a vertical convergence in the midlevels. Because the atmosphere is incompressible, vertical convergence leads to horizontal divergence flow that flows from center to perimeter. During the process of divergence, the circulation flow becomes anticyclonic due to Coriolis forcing, which always directs to the right side of motion in the Northern Hemisphere. This is the physical mechanism on how the anomalous surface land state

Unauthenticated | Downloaded 01/18/21 09:41 PM UTC

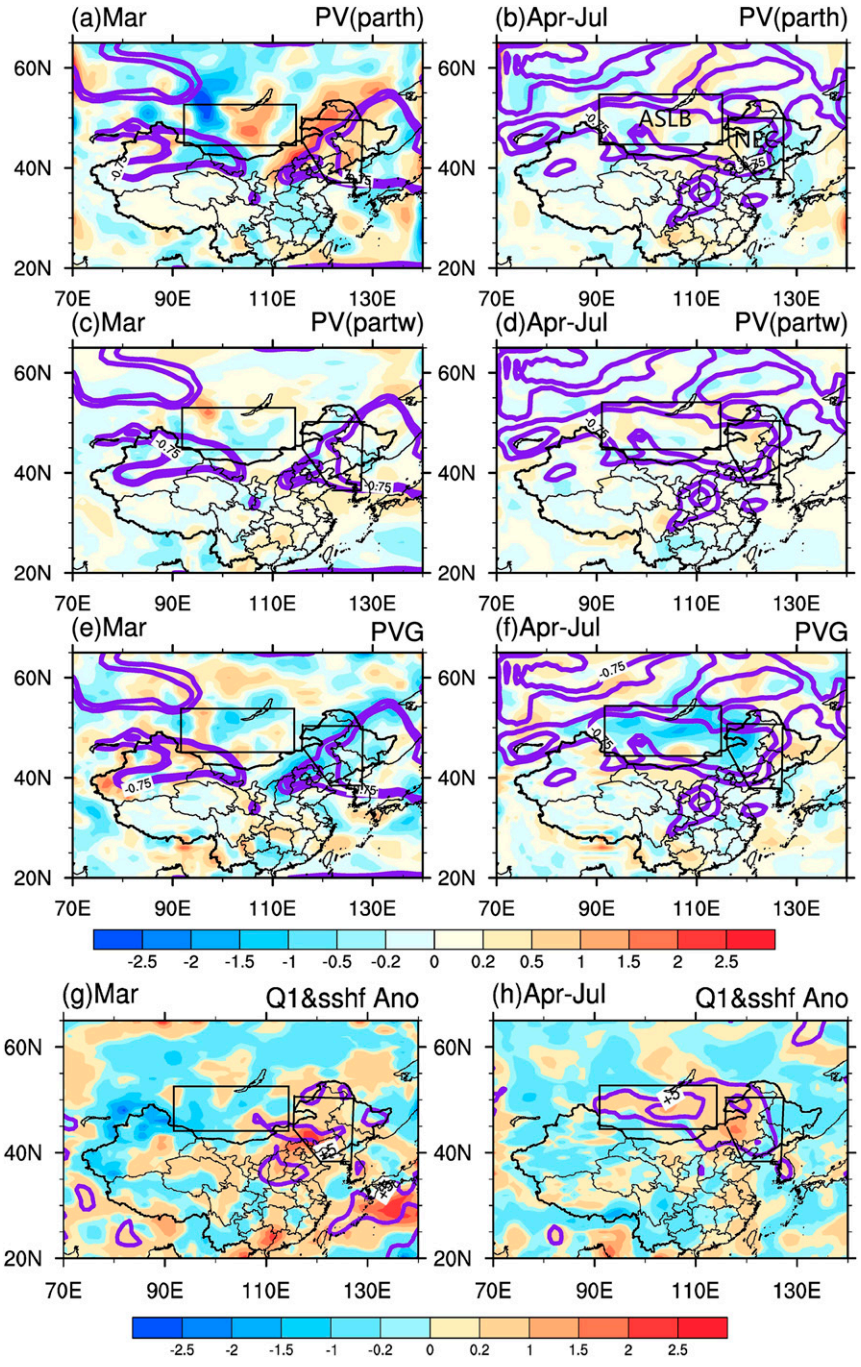

FIG. 6. The three terms related to the PV budget, (a),(b) part-h {horizontal advection term, $PV'_{part\text{-}h} = -[\overline{u}(\partial PV'/\partial x) + \overline{v}(\partial PV'/\partial y)] - [u'(\partial \overline{PV}/\partial x) + v'(\partial \overline{PV}/\partial y)]$; shaded; 10^{-1} PVU day^{-1}}, (c),(d) part-w [vertical advection term, $PV'_{part\text{-}w} = -\overline{\omega}(\partial PV'/\partial p) - \omega'(\partial \overline{PV}/\partial p)$; shaded; 10^{-1} PVU day^{-1}], and (e),(f) PVG [PV generation term due to vertical gradients of diabatic heating, $PV'_{PVG} = -g(f + \overline{\zeta})(\partial Q'_1/\partial p)$; shaded; 10^{-1} PVU day^{-1}] during March and April–July; contours in (a)–(f) are PV anomalies (10^{-1} PVU day^{-1}) in the corresponding period. (g),(h) The diabatic heating source Q_1 (shaded; K day^{-1}) and surface sensible heat flux (contours; W m^{-2}) anomalies.

Unauthenticated | Downloaded 01/18/21 09:41 PM UTC

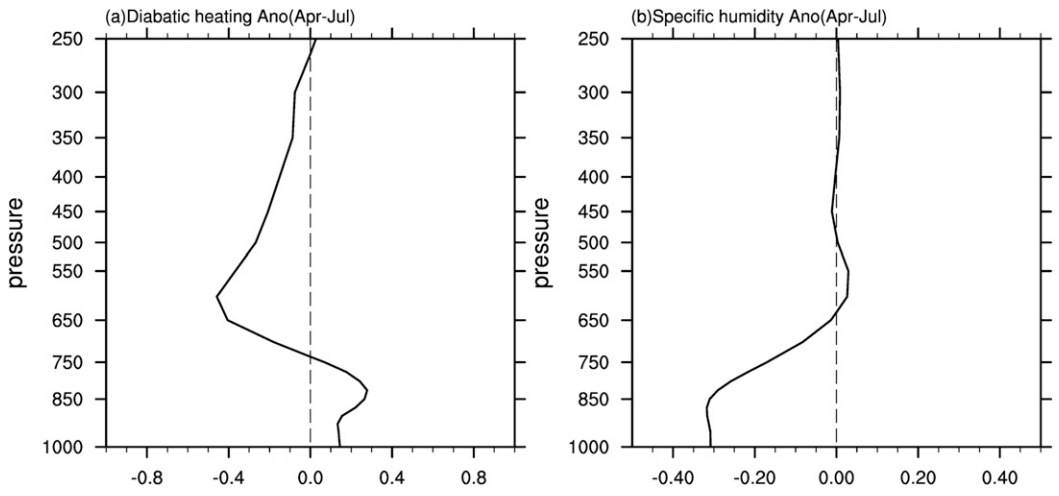

FIG. 7. Vertical profiles of (a) diabatic heating Q_1 anomalies (K day^{-1}) and (b) specific humidity anomalies (g kg^{-1}) averaged over the ASLB region marked in Fig. 5b.

provided feedback to the low-level atmospheric circulation during the persistent NEC drought.

d. *The relation between land–atmosphere coupling over ASLB and persistent drought events over NEC*

Reduced precipitation from spring to summer resulted in cumulative soil moisture deficits over ASLB. Whether this dry soil memory exerted influence on subsequent atmospheric circulation needs more investigation. Here, SVD analysis was performed between May (June) monthly SM (top 100 cm) and June (July) geopotential height (850 hPa) anomalies. The second component of the SVD for May SM and June geopotential height pattern (Figs. 9a,b) showed a reverse change over ASLB, which is similar to the corresponding anomalous pattern of soil moisture and geopotential height in 2017 (Fig. S2). This pattern explained 20% of the total variance, which is close to the explained variance by the first mode (26.9%), and the spatial patterns of soil moisture (Fig. 9a) and geopotential height (Fig. 9b) for the second component are more relevant to the drought series. The first component of the SVD of June SM and July geopotential height showed similar results, and explained

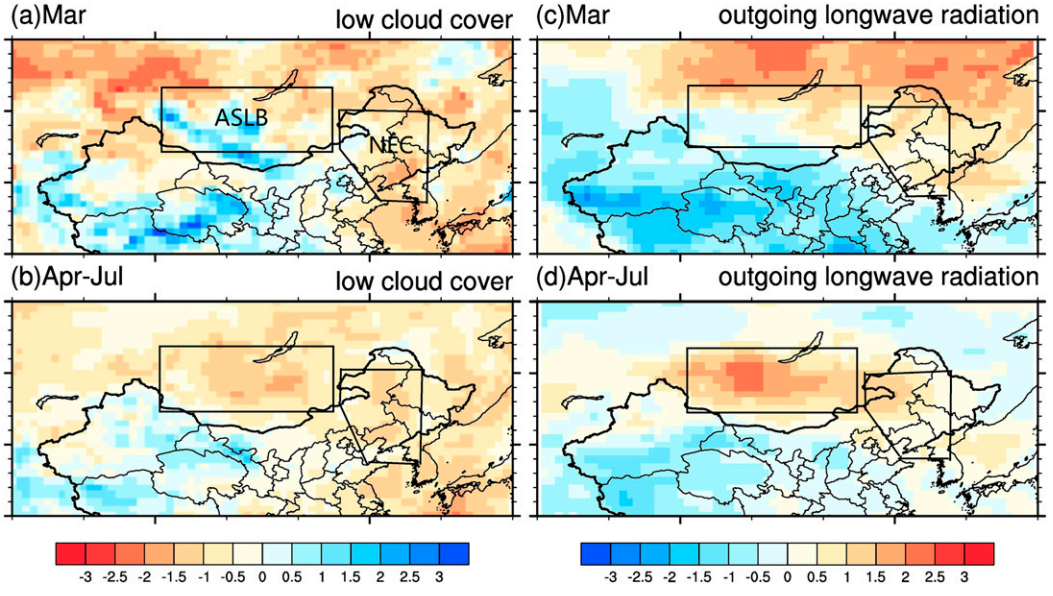

FIG. 8. Standardized anomalies of low cloud cover in (a) March and (b) April–July. (c),(d) As in (a) and (b), but for outgoing longwave radiation.

Unauthenticated | Downloaded 01/18/21 09:41 PM UTC

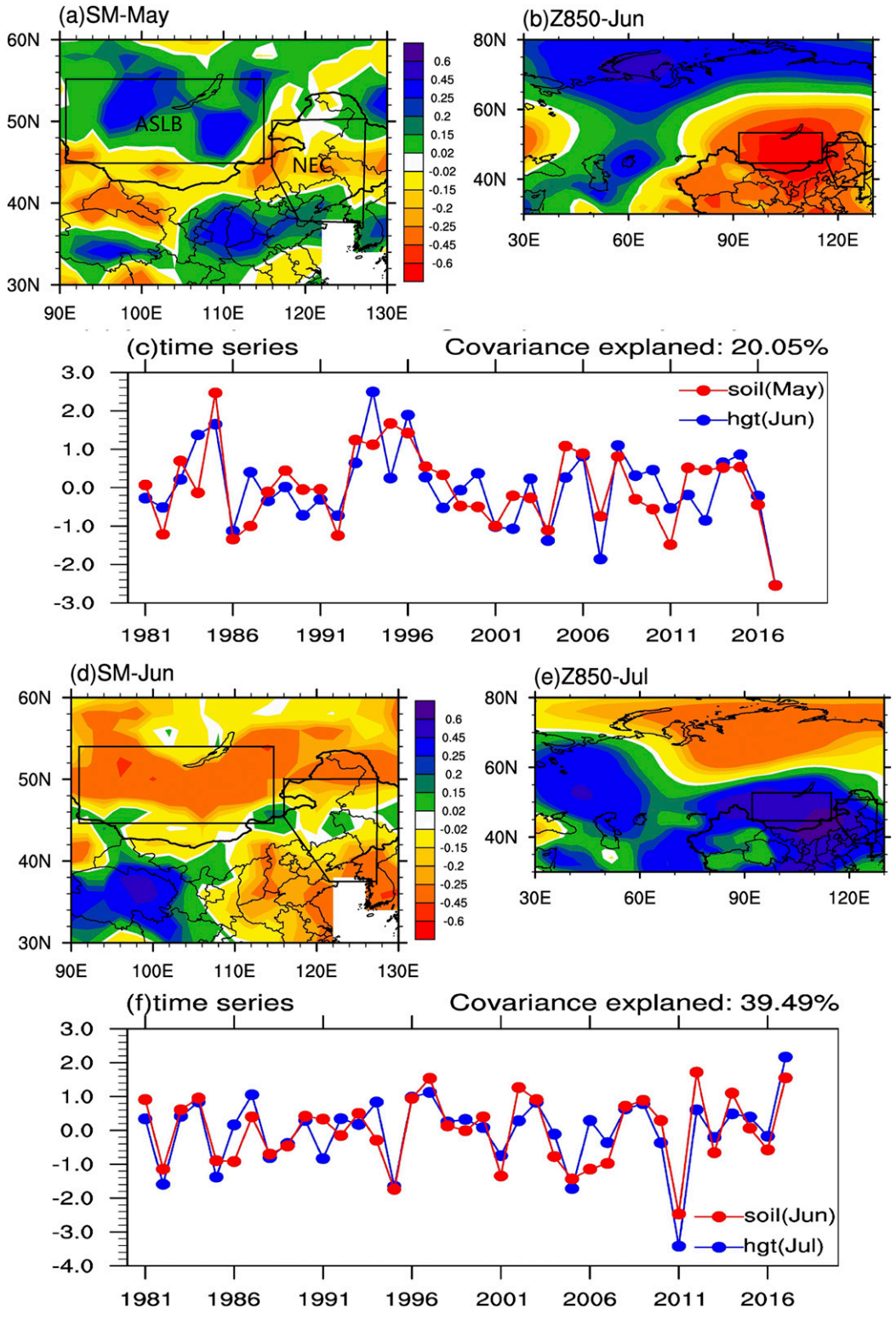

FIG. 9. (a)–(c) Heterogeneous correlation maps and their corresponding normalized time series of the second SVD modes for the normalized monthly top-100-cm soil moisture in May and 850-hPa geopotential height in June for the period of 1981–2017. (d)–(f) As in (a)–(c), but for the first SVD modes of soil moisture in June and geopotential height in July.

Unauthenticated | Downloaded 01/18/21 09:41 PM UTC

the most (39%) of the total variance (Figs. 9d,e). Both time series of the two patterns showed high correlation coefficients of 0.75 and 0.64, respectively, and showed extreme values in 2017 (Figs. 9c,f). This implies the soil moisture anomaly during May and June over ASLB is a key factor that influenced the local positive 850-hPa height anomalies one month later. We caution that statistical relationships between lagged variables, while suggestive, cannot prove causality.

The ASLB experienced the strongest dry coupling in 2017 (Fig. 5f), so the relationship between coupling and atmosphere circulation also requires further investigation. Correlation analysis for seasonal drought events suggests that the dry soil moisture may lead to a reduction in precipitation in later month through reducing evaporation (Wu and Kinter 2009). So we calculated the monthly regional average CDI time series over ASLB for May and June during 1981–2017, and correlated it with geopotential height and Q_1 (June and July) at 850 hPa with a one-month lag. Figure 10 shows that there is a significant positive correlation center over ASLB for geopotential height field (Fig. 10a) as well as the Q_1 field (Fig. 10b). The numerical experiments show that a stationary wave train can only maintain for three weeks as a response of idealized localized vorticity source forcing, or the internal atmospheric forcing (Schubert et al. 2011). External forcing from SST or soil moisture may play more important role in the maintenance of the wave train for longer time scales. To further study the response time of atmospheric circulation to the soil moisture anomaly, we calculated the lagged correlation between pentad mean 750-hPa meridional wind anomaly over NEC and soil moisture anomaly over ASLB (Fig. 11a), and found that there are significant positive correlations before 6–8 pentads, while the autocorrelation of meridional wind anomalies is lower and insignificant (Fig. 11b), indicating a connection between land surface anomaly and atmospheric drought. Han et al. (2017) demonstrated that there is a significant positive correlation between spring Niño-3 index and NEC summer precipitation, but there are weak negative correlations between Niño-3 and geopotential height at 500 hPa over ASLB and NEC. Moreover, the standardized Niño-3 index in 2017 spring is 0.66, which only shows a weak positive anomaly. So, the Niño SST anomaly may not be the reason for the 2017 NEC drought. The above correlation analysis suggests that as compared with the Niño SST anomaly, the terrestrial anomaly is more significantly related to the lower-level atmospheric circulation and thermodynamic conditions one month later.

We also selected other six persistent drought events over NEC during 1979–2017, with a standardized

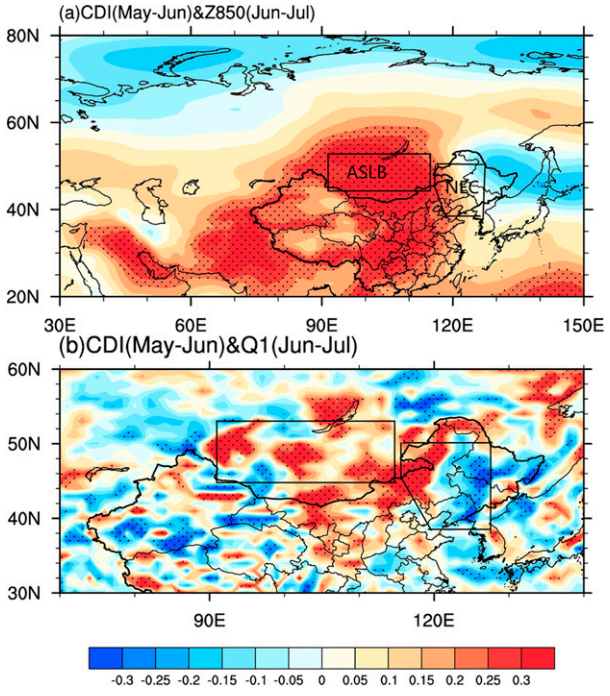

FIG. 10. (a) Lag correlation between time series of standardized CDI in May–June averaged over the ASLB region marked in Fig. 5b and monthly 850-hPa geopotential height field in June–July for the period of 1981–2017. (b) As in (a), but for lag correlation between CDI and diabatic heating source Q_1 field at 850 hPa; here the time series of CDI includes both the values of May and June instead of the average value of the two, as well as the Q_1 and geopotential height field, namely May vs June and June vs July separately.

precipitation anomaly in April–July lower than −1. These droughts occurred in 1982, 1987, 1997, 1999, 2000, and 2007. The composite result of these seven drought events (including 2017) shows similar circulation patterns as 2017 (Fig. 3b), where a mid–high-latitude teleconnection originated from the Atlantic with positive anomaly centers lying on the Atlantic and ASLB, negative center over the west coast of Europe (Fig. 12a). The composite result of PV budget at 750 hPa over ASLB shows positive anomaly of horizontal and vertical PV advections (shades in Figs. 12b and 12c), both terms give negative contribution to the negative PV anomaly (contours in Figs. 12b and 12c). The PVG (shades in Fig. 12d) term shows a negative center over ASLB, thus causes a positive contribution to the PV negative anomalous (contours in Fig. 12d), which is also consistent with the anomaly of 2017 (Figs. 6b,d,f). Likewise, the negative PVG anomaly is due to the positive vertical gradients of diabatic heating rate between 850 and 650 hPa with a maximal heating anomaly around 850 hPa and cooling around 650 hPa (Fig. 12f), the heating anomaly (shades in Fig. 12e) is caused by

Unauthenticated | Downloaded 01/18/21 09:41 PM UTC

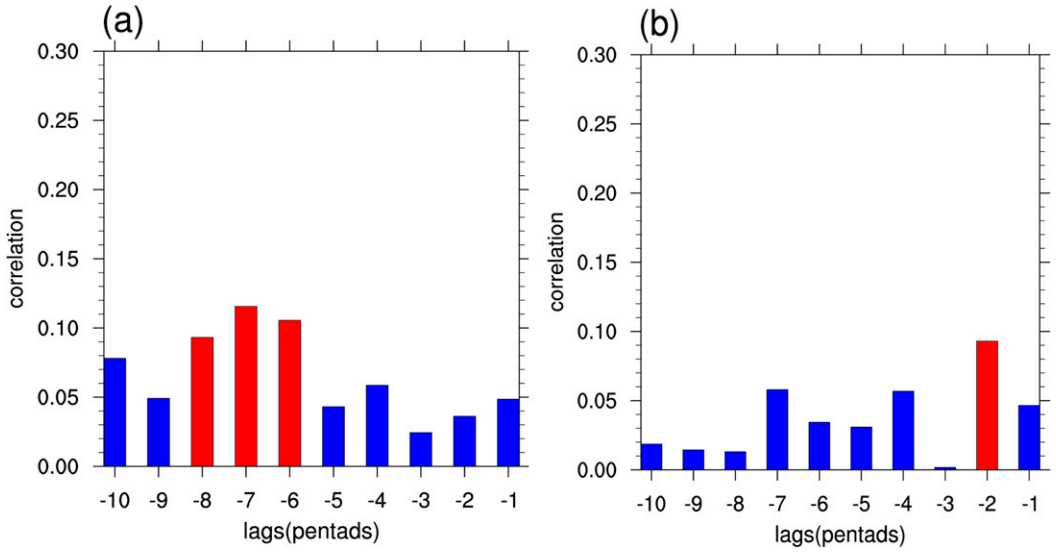

FIG. 11. (a) The lead correlation between pentad soil moisture anomalies (averaged over the ASLB region marked in Fig. 5b) and meridional wind anomalies of 750 hPa (averaged over the NEC region marked in Fig. 5b) during May–July (MJJ) over the period 1981–2017; the red bar denotes that the correlation value is statistically significant at the 5% level. (b) As in (a), but for the autocorrelation of meridional wind anomalies of 750 hPa over NEC.

the surface sensible flux (contours in Fig. 12e) and the cooling is caused by the decrease of cloud (not shown). The above composite results indicate that the phase-locking effect during persistent drought events is common over the NEC.

4. Conclusions and discussion

In this study, we diagnosed possible causes for the persistent extreme drought event in Northeast China (NEC) during March–July of 2017. The results showed that a strong positive phase of Arctic Oscillation (AO) in March triggered the NEC drought, and a teleconnection originating from the Atlantic maintained the negative precipitation anomaly during April–July with an anomalous anticyclonic circulation located over ASLB. Both the two patterns enhanced the Baikal high ridge and the associated dynamic descent, the north wind on the east side of the anticyclone weakened water vapor transport from the south, and these dynamical and water vapor conditions finally resulted in the extreme persistent NEC drought.

The land–atmosphere coupling over NEC and ASLB transitioned from wet coupling in March to dry coupling in April–July. A similar transition occurred in the fields of both soil moisture and atmosphere boundary layer. The record-breaking dry coupling during April–July of 2017 over ASLB led to a positive anomaly of surface sensible heating in the lower atmosphere. Meanwhile, a diabatic cooling anomaly formed in the upper level due to the decrease of low-level cloud cover caused by anomalous sinking motion. This anomalous vertical thermal structure led to a negative potential vorticity (PV) anomaly (anticyclone) in lower level over ASLB, and had a phase-locking effect on the teleconnection pattern originating from the Atlantic, indicating that the synergistic effect of upper barotropic processes and lower baroclinic processes led to the maintenance of anomalous anticyclone over ASLB, as well as the drought occurred over its downstream area (NEC) during April–July of 2017.

Over ASLB, drier soil during late spring and early summer corresponds to a higher geopotential height in the next month, and the dry coupling related diabatic heating in low level might be a key process for this relationship. The above conclusions demonstrate that the persistent ASLB anticyclonic anomaly is maintained by the combined influences of upstream Rossby wave and the local land–atmosphere coupling, which resulted in the downstream NEC drought in 2017. Our analysis shows a large-scale land–atmosphere feedback mechanism during persistent drought event, which may be helpful to understand the dynamic and thermodynamic processes for how the land state influences planetary waves in mid–high latitudes. Drought events can be promoted by positive thermodynamic feedbacks that favor depleted soil moisture and surface sensible heating. On the other hand, they are also strongly regulated by atmospheric dynamics that initiate and sustain anomalous heating and drying (Coumou et al. 2018). By conducting numerical simulations, Koster et al. (2016)

Unauthenticated | Downloaded 01/18/21 09:41 PM UTC

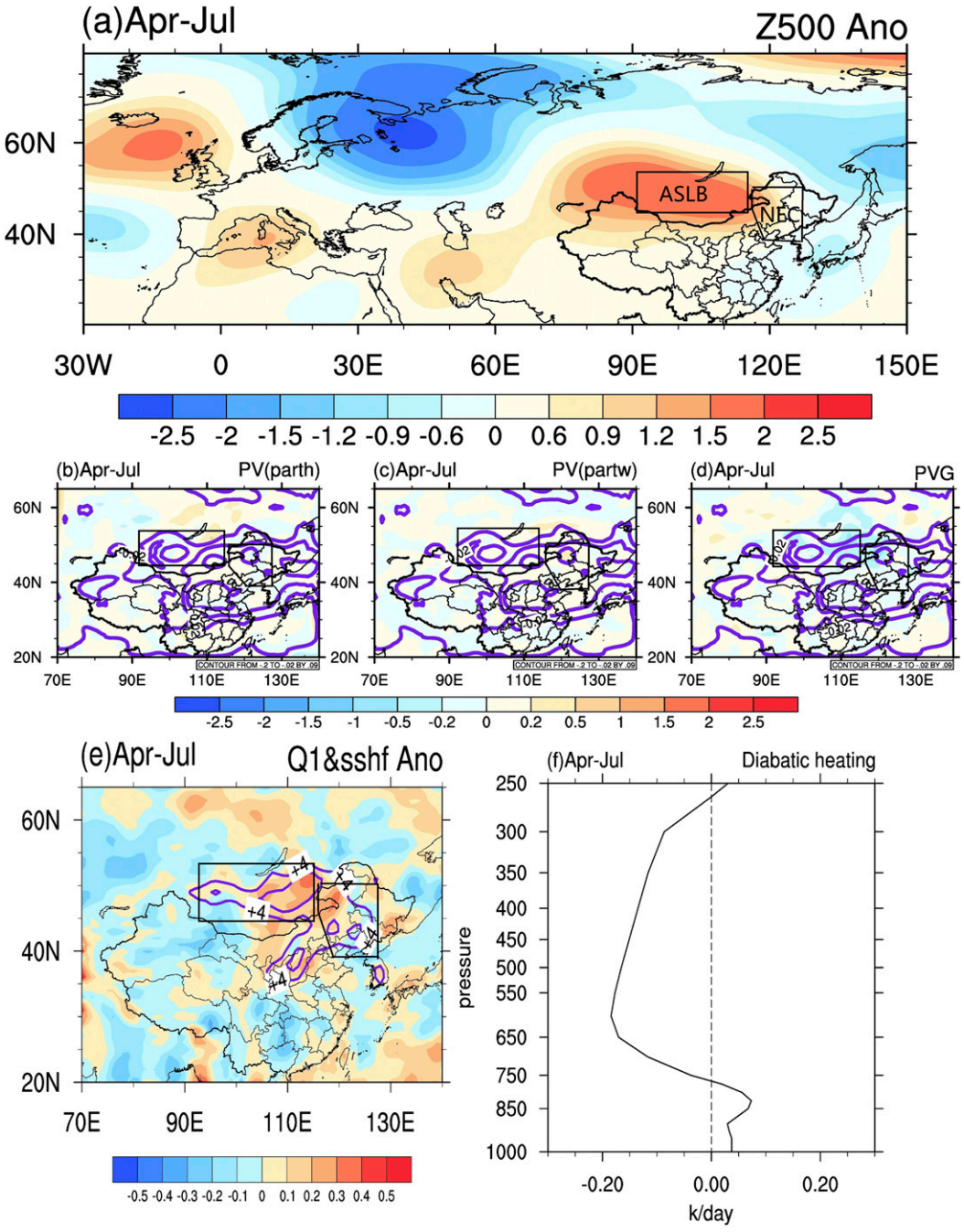

FIG. 12. The composite results of seven persistent drought events over NEC (standardized April–July mean precipitation anomaly over NEC less than −1). (a) Geopotential height anomalies (shaded; dagpm); (b)–(d) shaded are $PV'_{part\text{-}w}$, $PV'_{part\text{-}h}$ and PVG (10^{-1} PVU day^{-1}), and contours are PV anomalies (10^{-1} PVU day^{-1}); (e) the diabatic heating source Q_1 (shaded; K day^{-1}) and surface sensible heat flux (contour; W m^{-2}) anomalies and (f) vertical profiles of diabatic heating Q_1 anomalies (K day^{-1}) over ASLB.

shows that cumulative surface dryness in the U.S. interior can excite an anticyclonic anomaly over the west-central United States, and this circulation condition is favorable to sensible heating of atmosphere which in turn maintains the upper circulation. Further study shows that the phase locking also depends on the local atmospheric basic state (H. Wang et al. 2019). Moreover, dry surface conditions can also enhance the positive height anomaly at upper levels and thus make it more persistent during the 2003 European summer heat

Unauthenticated | Downloaded 01/18/21 09:41 PM UTC

wave (Fischer et al. 2007). These previous studies show an apparent phase-locking and amplification effect of soil moisture dryness on the upper atmosphere circulation. Here we analyzed the combined effect of surface heating and upper-level cooling on the Rossby wave originating from upstream, and speculate that this drought mechanism may also be relevant for Europe and the United States, as well as other hot spots of atmosphere–land coupling over the midlatitudes of the Northern Hemisphere.

Soil moisture, the atmospheric boundary layer, and the free atmosphere are highly coupled to each other. Soil moisture dryness influences the atmospheric circulation through changing the thermodynamic condition in boundary layer, so the qualitative study on this effect can be conducted through forcing an ideal model by an artificial vertical heating profile with a maximum diabatic heating rate at lower levels, which can be regarded as the anomalous diabatic heating induced by surface sensible heat (Koster et al. 2014, 2016). Numerous studies based on realistic models also try to isolate and quantify the feedback from surface to atmosphere: Zhang and Wu (2011) do a GLACE1-type coupling experiment with Weather Research and Forecasting Model, and found that land–atmosphere coupling generally accounts for 30%–70% of the numbers of hot days and heat waves over eastern and southwestern China. In our future work, we will try to do a similar simulation to isolate the effect of land–atmosphere coupling and teleconnection on the local atmosphere circulation.

Furthermore, precipitation in NEC is also modulated by the NAO and the PDO, with the East Asian summer monsoon varying at interannual to decadal time scales, respectively (Sun and Wang 2012; Li et al. 2010). Therefore, the regulation of large-scale orography (the Tibetan Plateau), NAO, and PDO on land–atmosphere coupling deserves to be further investigated.

Acknowledgments. This work was supported by National Key R&D Program of China (2018YFA0606002), National Natural Science Foundation of China (41875105, 41861124005), and China Special Fund for Meteorological Research in the Public Interest (major projects) (GYHY201506001).

REFERENCES

Chen, M., P. Xie, and J. E. Janowiak, 2002: Global land precipitation: A 50-yr monthly analysis based on gauge observations. *J. Hydrometeor.*, **3**, 249–266., https://doi.org/10.1175/1525-7541(2002)003<0249:GLPAYM>2.0.CO;2.

Chen, Z., and G. Yang, 2013: Analysis of drought hazards in north China: Distribution and interpretation. *Nat. Hazards*, **65**, 279–294, https://doi.org/10.1007/s11069-012-0358-3.

Coumou, D., G. Di Capua, S. Vavrus, L. Wang, and S. Wang, 2018: The influence of Arctic amplification on mid-latitude summer circulation. *Nat. Commun.*, **9**, 2959, https://doi.org/10.1038/s41467-018-05256-8.

Dee, D. P., and Coauthors, 2011: The ERA-Interim reanalysis: Configuration and performance of the data assimilation system. *Quart. J. Roy. Meteor. Soc.*, **137**, 553–597, https://doi.org/10.1002/qj.828.

Ding, Y., Y. Sun, Z. Wang, Y. Zhu, and Y. Song, 2009: Interdecadal variation of the summer precipitation in China and its association with decreasing Asian summer monsoon. Part II: Possible causes. *Int. J. Climatol.*, **29**, 1926–1944, https://doi.org/10.1002/joc.1759.

Dirmeyer, P. A., and S. Halder, 2017: Application of the land–atmosphere coupling paradigm to the operational Coupled Forecast System, version 2 (CFSv2). *J. Hydrometeor.*, **18**, 85–108, https://doi.org/10.1175/JHM-D-16-0064.1.

Findell, K. L., and E. A. B. Eltahir, 2003a: Atmospheric controls on soil moisture–boundary layer interactions. Part I: Framework development. *J. Hydrometeor.*, **4**, 552–569, https://doi.org/10.1175/1525-7541(2003)004<0552:ACOSML>2.0.CO;2.

Fischer, E. M., S. I. Seneviratne, P. L. Vidale, D. Luthi, and C. Schar, 2007: Soil moisture–atmosphere interactions during the 2003 European summer heat wave. *J. Climate*, **20**, 5081–5099, https://doi.org/10.1175/JCLI4288.1.

Han, T., H. Chen, and H. Wang, 2015: Recent changes in summer precipitation in northeast China and the background circulation. *Int. J. Climatol.*, **35**, 4210–4219, https://doi.org/10.1002/joc.4280.

——, H. Wang, and J. Sun, 2017: Strengthened relationship between eastern ENSO and summer precipitation over northeastern China. *J. Climate*, **30**, 4497–4512, https://doi.org/10.1175/JCLI-D-16-0551.1.

Jin, D., Z. Guan, and W. Tang, 2013: The extreme drought event during winter–spring of 2011 in East China: Combined influences of teleconnection in midhigh latitudes and thermal forcing in maritime continent region. *J. Climate*, **26**, 8210–8222, https://doi.org/10.1175/JCLI-D-12-00652.1.

Koster, R. D., Y. Chang, and S. Schubert, 2014: A mechanism for land–atmosphere feedback involving planetary wave structures. *J. Climate*, **27**, 9290–9301, https://doi.org/10.1175/JCLI-D-14-00315.1.

——, ——, H. Wang, and S. Schubert, 2016: Impacts of local soil moisture anomalies on the atmospheric circulation and on remote surface meteorological fields during boreal summer: A comprehensive analysis over North America. *J. Climate*, **29**, 7345–7363, https://doi.org/10.1175/JCLI-D-16-0192.1.

Li, H., A. Dai, T. Zhou, and J. Lu, 2010: Responses of East Asian summer monsoon to historical SST and atmospheric forcing during 1950–2000. *Climate Dyn.*, **34**, 501–514, https://doi.org/10.1007/s00382-008-0482-7.

——, H. Chen, H. Wang, J. Sun, and J. Ma, 2018: Can Barents Sea ice decline in spring enhance summer hot drought events over northeastern China? *J. Climate*, **31**, 4705–4724, https://doi.org/10.1175/JCLI-D-17-0429.1.

Li, Y., H. Xu, and D. Liu, 2011: Features of the extremely severe drought in the east of southwest China and anomalies of atmospheric circulation in summer 2006. *Acta Meteor. Sin.*, **25**, 176–187, https://doi.org/10.1007/s13351-011-0025-8.

——, and Coauthors, 2019: Mechanisms and early warning of drought disasters: Experimental drought meteorology research over

Unauthenticated | Downloaded 01/18/21 09:41 PM UTC

China. *Bull. Amer. Meteor. Soc.*, **100**, 673–687, https://doi.org/10.1175/BAMS-D-17-0029.1.

Liebmann, B., and C. A. Smith, 1996: Description of a complete (interpolated) outgoing longwave radiation dataset. *Bull. Amer. Meteor. Soc.*, **77**, 1275–1277, https://doi.org/10.1175/1520-0477-77.6.1274.

Lu, R. Y., J. H. Oh, and B. J. Kim, 2002: A teleconnection pattern in upper-level meridional wind over the North African and Eurasian continent in summer. *Tellus*, **54A**, 44–55, https://doi.org/10.1034/j.1600-0870.2002.00248.x.

Nitta, T., 1987: Convective activities in the tropical western Pacific and their impact on the Northern Hemisphere summer circulation. *J. Meteor. Soc. Japan*, **62**, 165–171, https://doi.org/10.2151/JMSJ1965.65.3_373.

Ren, X., D. Yang, and X. Yang, 2015: Characteristics and mechanisms of the subseasonal eastward extension of the South Asian high. *J. Climate*, **28**, 6799–6822, https://doi.org/10.1175/JCLI-D-14-00682.1.

Roundy, J. K., C. R. Ferguson, and E. F. Wood, 2013: Temporal variability of land–atmosphere coupling and its implications for drought over the southeast United States. *J. Hydrometeor.*, **14**, 622–635, https://doi.org/10.1175/JHM-D-12-090.1.

Santanello, J. A., C. D. Peters-Lidard, and S. V. Kumar, 2011: Diagnosing the sensitivity of local land–atmosphere coupling via the soil moisture–boundary layer interaction. *J. Hydrometeor.*, **12**, 766–786, https://doi.org/10.1175/JHM-D-10-05014.1.

Schubert, S. D., H. Wang, and M. Suarez, 2011: Warm season subseasonal variability and climate extremes in the Northern Hemisphere: The role of stationary Rossby waves. *J. Climate*, **24**, 4773–4792, https://doi.org/10.1175/JCLI-D-10-05035.1.

——, ——, R. D. Koster, M. J. Suarez, and P. Ya. Groisman, 2014: Northern Eurasian heat waves and droughts. *J. Climate*, **27**, 3169–3207, https://doi.org/10.1175/JCLI-D-13-00360.1.

Sun, J., and H. Wang, 2012: Changes of the connection between the summer North Atlantic Oscillation and the East Asian summer rainfall. *J. Geophys. Res.*, **117**, D08110, https://doi.org/10.1029/2011JA017106.

Takaya, K., and H. Nakamura, 2001: A formulation of a phase-independent wave-activity flux for stationary and migratory quasigeostrophic eddies on a zonally varying basic flow. *J. Atmos. Sci.*, **58**, 608–627, https://doi.org/10.1175/1520-0469(2001)058<0608:AFOAPI>2.0.CO;2.

Thompson, D. W. J., and J. M. Wallace, 1998: The Arctic Oscillation signature in the wintertime geopotential height and temperature fields. *Geophys. Res. Lett.*, **25**, 1297–1300, https://doi.org/10.1029/98GL00950.

Wallace, J. M., and D. S. Gutzler, 1981: Teleconnection in the geopotential height field during the Northern Hemisphere winter. *Mon. Wea. Rev.*, **109**, 784–812, https://doi.org/10.1175/1520-0493(1981)109<0784:TITGHF>2.0.CO;2.

Wang, H. J., 2001: The weakening of the Asian monsoon circulation after the end of 1970s. *Adv. Atmos. Sci.*, **18**, 376–386, https://doi.org/10.1007/BF02919316.

——, and S. He, 2015: The north China/northeastern Asia severe summer drought in 2014. *J. Climate*, **28**, 6667–6681, https://doi.org/10.1175/JCLI-D-15-0202.1.

Wang, H. L., S. D. Schubert, R. D. Koster, and Y. Chang, 2019: Phase locking of the boreal summer atmospheric response to dry land surface anomalies in the Northern Hemisphere. *J Climate*, **32**, 1081–1099, https://doi.org/10.1175/JCLI-D-18-0240.1.

Wang, S., X. Yuan, and Y. Li, 2017: Does a strong El Niño imply a higher predictability of extreme drought? *Sci. Rep.*, **7**, 40 741, https://doi.org/10.1038/srep40741.

——, ——, and R. Wu, 2019: Attribution of the persistent spring–summer hot and dry extremes over Northeast China in 2017 [in "Explaining Extreme Events of 2017 from a Climate Perspective"]. *Bull. Amer. Meteor. Soc.*, **100** (1), S85–S89, https://doi.org/10.1175/BAMS-D-18-0120.1.

Wei, J., Q. Y. Zhang, and S. Y. Tao, 2004: Physical causes of the 1999 and 2000 summer severe drought in North China (in Chinese). *Chin. J. Atmos. Sci.*, **28**, 125–137.

Wu, R., and J. L. Kinter III, 2009: Analysis of the relationship of U.S. droughts with SST and soil moisture: Distinguishing the time scale of droughts. *J. Climate*, **22**, 4250–4538, https://doi.org/10.1175/2009JCLI2841.1.

Xu, Z., K. Fan, and H. Wang, 2017: Role of sea surface temperature anomalies in the tropical Indo-Pacific region in the northeast Asia severe drought in summer 2014: Month-to-month perspective. *Climate Dyn.*, **49**, 1631–1650, https://doi.org/10.1007/s00382-016-3406-y.

Yanai, M., and T. Tomita, 1998: Seasonal and interannual variability of atmospheric heat sources and moisture sinks as determined from NCEP–NCAR reanalysis. *J. Climate*, **11**, 463–482, https://doi.org/10.1175/1520-0442(1998)011<0463:SAIVOA>2.0.CO;2.

Yang, J., D. Gong, W. Wang, M. Hu, and R. Mao, 2012: Extreme drought event of 2009/2010 over southwestern China. *Meteor. Atmos. Phys.*, **115**, 173–184, https://doi.org/10.1007/s00703-011-0172-6.

Yin, S., J. Feng, and J. Li, 2013: Influence of the preceding winter Northern Hemisphere annular mode on the spring extreme low temperature events in the north of eastern China. *Acta Meteor. Sin.*, **71**, 96–108, https://doi.org/10.11676/qxxb2013.008.

Yu, R., B. Wang, and T. Zhou, 2004: Tropospheric cooling and summer monsoon weakening trend over East Asia. *Geophys. Res. Lett.*, **31**, L22212, https://doi.org/10.1029/2004GL021270.

Yuan, X., and E. F. Wood, 2013: Multimodel seasonal forecasting of global drought onset. *Geophys. Res. Lett.*, **40**, 4900–4905, https://doi.org/10.1002/grl.50949.

Zeng, D., and X. Yuan, 2018: Multiscale land–atmosphere coupling and its application in assessing subseasonal forecasts over East Asia. *J. Hydrometeor.*, **19**, 745–760, https://doi.org/10.1175/JHM-D-17-0215.1.

Zhang, J., and L. Wu, 2011: Land–atmosphere coupling amplifies hot extremes over China. *Chin. Sci. Bull.*, **56**, https://doi.org/10.1007/S11434-011-4628-3.

Zhang, L., P. Wu, T. Zhou, and C. Xiao, 2018: ENSO transition from La Niña to El Niño drives prolonged spring–summer drought over North China. *J. Climate*, **31**, 3509–3523, https://doi.org/10.1175/JCLI-D-17-0440.1.

Zhang, Y., L. Zhang, S. P. Wang, and J. Feng, 2017: Drought events and their influence in summer of 2017 in China (in Chinese). *J. Arid Meteor.*, **35**, 899–905.

Zhou, T., D. Gong, J. Li, and B. Li, 2009: Detecting and understanding the multi-decadal variability of the East Asian summer monsoon—Recent progress and state of affairs. *Meteor. Z.*, **18**, 455–467, https://doi.org/10.1127/0941-2948/2009/0396.

Unauthenticated | Downloaded 01/18/21 09:41 PM UTC